

This is a pre print version of the following article:

A Continuum Model for Circular Graphene Membranes Under Uniform Lateral Pressure / Pelliciari, M; Tarantino, Am. - In: JOURNAL OF ELASTICITY. - ISSN 0374-3535. - 151:2(2022), pp. 273-303. [10.1007/s10659-022-09937-w]

*Terms of use:*

The terms and conditions for the reuse of this version of the manuscript are specified in the publishing policy. For all terms of use and more information see the publisher's website.

05/01/2026 20:44

# A continuum model for circular graphene membranes under uniform lateral pressure

Matteo Pellicciari · Angelo Marcello Tarantino

Received: - / Accepted: -

**Abstract** Despite the numerous applications of pressurized graphene membranes in new technologies, there is still a lack of accurate mechanical models. In this work we propose a continuum model for circular graphene membranes subjected to uniform lateral pressure. We adopt a semi-inverse method by defining the kinematics of deformation and we describe the material behavior with a stored energy function that takes into account both nonlinearity and anisotropy of graphene. From the equilibrium we obtain an expression of the applied pressure as a function of the deflection of the membrane. A finite element (FE) model in nonlinear elasticity is presented and the results are used to validate the analytical model. A comparison with other models, numerical simulations and experiments from the literature demonstrates the advantages of the model proposed in this work. Differently from our entirely nonlinear approach, all the continuum models in the literature are based on the assumption of linear elastic material, which is suitable only when deformations are small. The present model gives a comprehensive description of the mechanics of pressurized graphene membranes.

**Keywords** Graphene membrane · Nonlinear elasticity · Anisotropy · Hyperelasticity · Finite element

**Mathematics Subject Classification (2010)** 74B20 · 74G05 · 74K15 · 74S05 · 74E10

## 1 Introduction

Numerous applications in new technologies involve the use of graphene. The extraordinary mechanical, thermal and electrical properties of this material attracted the interest of researchers from many engineering fields. In fact, graphene is used in micro-and nano-electronic devices [37, 46], biomedicine [38], nanocomposite materials [5, 27, 36], energy generation and storage [33, 35], electrochemical sensors [14], and many other applications.

Graphene membranes are impermeable to standard gases and therefore they are often used for pressure sensors [2]. Pressurized graphene membranes provide a one-atom-thick separation barrier that can support large

---

M. Pellicciari  
DIEF, Department of Engineering “Enzo Ferrari”, via Pietro Vivarelli 10, 41125 Modena, Italy  
Tel.: +39 3334858333  
E-mail: matteo.pellicciari@unimore.it

A. M. Tarantino  
DIEF, Department of Engineering “Enzo Ferrari”, via Pietro Vivarelli 10, 41125 Modena, Italy  
E-mail: angelomarcello.tarantino@unimore.it

pressure differences. Liu et al. [21] reported the outstanding molecular separation properties of graphene membranes, which can be applied to pressure filtration, pervaporation and gas separation. Graphene membranes are also used as piezoresistive pressure sensors [48] and as pressure sensors for detecting human motions [39]. Wang et al. [43] presented a graphene-based microelectromechanical system (MEMS) pressure sensor and showed that, thanks to its high sensitivity, it outperforms most existing MEMS sensors. Moreover, polymer nanocomposite membranes based on graphene find new and promising technological applications [15, 24].

Despite the enormous potential of pressurized graphene membranes, there is still a lack of accurate mechanical models. Wang et al. [42] analyzed the problem of circular graphene membranes subjected to uniform lateral pressure and proposed approximated analytical solutions based on the assumption of linear elastic material. They carried out molecular dynamics simulations on a nanoscale membrane and it was found that the approximated solutions are suitable only for small deflections (linear elasticity). Jiang et al. [13] and Wang et al. [40] carried out FE simulations by modeling the graphene sheet with, respectively, plate and shell elements composed of linear elastic material. Li et al. [20] proposed a continuum model based on the large deflection elastic theory of circular membranes and investigated the effect of variations of the membrane parameters by using FE simulations.

The above models are all based on the hypothesis of linear elastic constitutive response of graphene. However, experiments and numerical simulations showed that graphene exhibits a pronounced material nonlinearity, which derives from the nonlinear carbon-carbon interactions in the hexagonal lattice [19, 22, 30, 32]. In addition, graphene is isotropic only for infinitesimal deformations, while in the theory of large deformations its anisotropy must be taken into account [12]. This behavior of graphene is not considered in the models mentioned above. Against this background, there are still important issues that must be addressed to provide a comprehensive description of the mechanics of circular pressurized graphene membranes.

In the present work, we derive a solution to this problem in finite elasticity. We adopt a semi-inverse method by defining the kinematics of deformation of the circular pressurized membrane. Consequently, we consider the anisotropic hyperelastic material model for graphene proposed by Höller et al. [11] and we derive the stress measures. The equilibrium is then written and an expression of the applied pressure as a function of the deflection of the central point of the membrane is derived. Differently from the other models in the literature, the material nonlinearity of graphene is accurately described.

The proposed analytical model is validated with the results of a FE simulation. The FE simulation was carried out in software COMSOL Multiphysics. Both material and geometric nonlinearities were considered. After validating the model, we present a comparison with other results from experiments and simulations found in the literature. The comparison demonstrates the advantages of the present model and points out the importance of considering the nonlinear material response of graphene.

The model proposed in this work represents a straightforward tool for an accurate analysis of the mechanics of pressurized graphene membranes. Having at hand a direct expression of pressure as a function of deflection is a great advantage. Instead, atomistic and FE simulations are complex and require high computational effort.

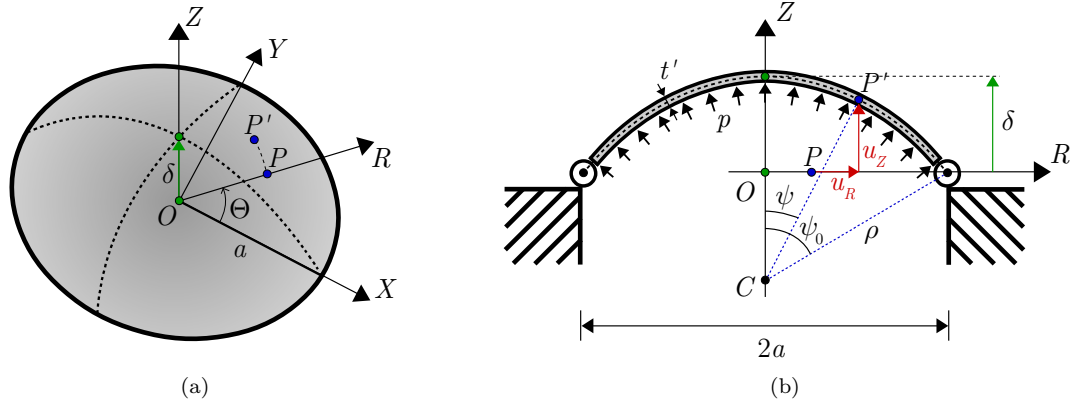


Fig. 1: (a) Circular graphene membrane subjected to uniform lateral pressure and (b) kinematics of deformation in the  $R$ - $Z$  plane based on the assumption that the membrane transforms into a spherical cap with origin in  $C$ .

Especially atomistic simulations, which are accurate but can be applied only to systems composed of a small number of atoms.

The paper is organized as follows. The hyperelastic model for circular graphene membranes under uniform lateral pressure is presented in Section 2. The FE model is described in Section 3. The results are given in Section 4, where we first validate the model and subsequently we present a comparison with other results from the literature. Conclusions are drawn in Section 5.

## 2 Hyperelastic model for circular graphene membranes subjected to uniform lateral pressure

The circular pressurized graphene membrane is depicted in Fig. 1a. The undeformed flat membrane has radius  $a$  and thickness  $t$ . We introduce a Cartesian coordinate system  $(X, Y, Z)$  and a cylindrical coordinate system  $(R, \Theta, Z)$ , both with origin in  $O$ . Directions  $X$  and  $Y$  correspond respectively to zigzag and armchair directions in the graphene hexagonal lattice [3, 17]. The membrane is subjected to the uniform pressure  $p$  and material point  $P$  moves to  $P'$ . We assume that the membrane preserves its rotational symmetry after deformation, therefore  $\Theta' = \Theta$ . The coordinates of  $P'$  in deformed configuration are  $(R', \Theta, Z')$ .

We assume that the initially flat membrane transforms into a spherical cap. Note that the ultimate strain of graphene subjected to uniaxial elongation is around 15-20% [41, 44, 47]. Since the deformations involved are moderately large, the assumption that the membrane transforms into a spherical cap gives an appropriate description of the kinematics of deformation [45]. This hypothesis will be validated by the FE simulation of Section 3.

The membrane deforms according to the kinematics of Fig. 1b. The spherical cap is centered in point  $C$  and has radius  $\rho$ . Displacement field  $\mathbf{u}(P)$  of point  $P$  with coordinates  $(R, \Theta, 0)$  has the following expression



in cylindrical coordinates:

$$\begin{aligned} u_R(P) &= R' - R = \rho \sin \psi - R, \\ u_\Theta(P) &= 0, \\ u_Z(P) &= Z' = \rho (\cos \psi - \cos \psi_0), \end{aligned}$$

where  $\psi_0 \in (0, \pi)$  and

$$\rho = \frac{a}{\sin \psi_0}, \quad \psi = \frac{\psi_0 R}{a}.$$

The deformation of point  $P$  is  $\boldsymbol{\varphi}(P) = \mathbf{id}(P) + \mathbf{u}(P)$ <sup>1</sup> and its representation in cylindrical coordinates is

$$\begin{aligned} \varphi_R(P) &= \rho \sin \psi, \\ \varphi_\Theta(P) &= \Theta, \\ \varphi_Z(P) &= \rho (\cos \psi - \cos \psi_0). \end{aligned}$$

In order to derive the deformation gradient  $\mathbf{F}$  we must introduce the contraction of the membrane thickness, which is expressed by stretch  $\lambda_Z$ . However, we are considering a single-layer graphene sheet whose thickness corresponds to the diameter of the carbon atom. From a physical point of view it is not possible that such thin membrane undergoes a transverse contraction, because it would produce a reduction of the dimension of the atom. In light of this, the only possible and reasonable assumption is that  $\lambda_Z = 1$  throughout the deformation process. Hence, thickness  $t$  of the undeformed membrane remains unchanged ( $t' = t$ ). The deformation gradient is thus derived as follows:

$$[\mathbf{F}] = \begin{bmatrix} \frac{\partial \varphi_R}{\partial R} & \frac{1}{R} \frac{\partial \varphi_R}{\partial \Theta} & \sin \psi \\ \varphi_R \frac{\partial \varphi_\Theta}{\partial R} & \frac{\varphi_R}{R} \frac{\partial \varphi_\Theta}{\partial \Theta} & 0 \\ \frac{\partial \varphi_Z}{\partial R} & \frac{1}{R} \frac{\partial \varphi_Z}{\partial \Theta} & \cos \psi \end{bmatrix} = \begin{bmatrix} \rho \frac{\partial \psi}{\partial R} \cos \psi & 0 & \sin \psi \\ 0 & \frac{\rho \sin \psi}{R} & 0 \\ -\rho \frac{\partial \psi}{\partial R} \sin \psi & 0 & \cos \psi \end{bmatrix}.$$

The polar decomposition of the deformation gradient,  $\mathbf{F} = \mathbf{R}\mathbf{U}$ , allows us to write rotation tensor  $\mathbf{R}$  and pure deformation tensor  $\mathbf{U}$  as

$$[\mathbf{R}] = \begin{bmatrix} \cos \psi & 0 & \sin \psi \\ 0 & 1 & 0 \\ -\sin \psi & 0 & \cos \psi \end{bmatrix}, \quad [\mathbf{U}] = \begin{bmatrix} \rho \frac{\partial \psi}{\partial R} & 0 & 0 \\ 0 & \frac{\rho \sin \psi}{R} & 0 \\ 0 & 0 & 1 \end{bmatrix}. \quad (1)$$

Tensor  $\mathbf{U}$  is diagonal and therefore the cylindrical coordinate system  $(R, \Theta, Z)$  is principal. Hence, from (1) we derive the following expressions of the principal stretches:

$$\lambda_R = \rho \frac{\partial \psi}{\partial R} = \frac{\rho \psi_0}{a}, \quad \lambda_\Theta = \frac{\rho \sin \psi}{R}. \quad (2)$$

---

<sup>1</sup>  $\mathbf{id}(P)$  indicates the position vector of point  $P$ .

Radial stretch  $\lambda_R$  is not a function of position because we assumed that the membrane deforms into a spherical cap.

The right Cauchy-Green deformation tensor,  $\mathbf{C} = \mathbf{F}^T \mathbf{F}$ , is computed and expressed in cylindrical coordinates

as

$$[\mathbf{C}] = \begin{bmatrix} \lambda_R^2 & 0 & 0 \\ 0 & \lambda_\Theta^2 & 0 \\ 0 & 0 & 1 \end{bmatrix},$$

with  $\lambda_R$  and  $\lambda_\Theta$  given by (2). The Green-Lagrange strain tensor,  $\mathbf{E} = (\mathbf{C} - \mathbf{I})/2$ , has the following diagonal form:

$$[\mathbf{E}] = \begin{bmatrix} E_R & 0 & 0 \\ 0 & E_\Theta & 0 \\ 0 & 0 & E_Z \end{bmatrix} = \frac{1}{2} \begin{bmatrix} \lambda_R^2 - 1 & 0 & 0 \\ 0 & \lambda_\Theta^2 - 1 & 0 \\ 0 & 0 & 0 \end{bmatrix}. \quad (3)$$

The extensive number of investigations on the mechanical behavior of graphene demonstrated that this material is isotropic only for small deformations, while anisotropy arises when deformations become large [12, 26]. This is due to the particular symmetry and periodicity of the graphene honeycomb lattice. To this regard, Kumar and Parks [18] used the isotropicization theorem [34] to define an additional invariant of the Green-Lagrange strain tensor that reproduces the anisotropic nature of graphene. We introduce tensors  $\mathbf{M} = \mathbf{n}_X \otimes \mathbf{n}_X - \mathbf{n}_Y \otimes \mathbf{n}_Y$ <sup>2</sup> and  $\mathbf{N} = \mathbf{n}_X \otimes \mathbf{n}_Y + \mathbf{n}_Y \otimes \mathbf{n}_X$ , which define the material symmetry group of graphene. Thereby, the strain energy density of graphene is written as a function of the following strain invariants:

$$\begin{aligned} I_1 &= \text{tr} \mathbf{E} = E_R + E_\Theta, \\ I_2 &= \frac{1}{2} \left[ (\text{tr} \mathbf{E})^2 - \text{tr} (\mathbf{E}^2) \right] = E_R E_\Theta, \\ I_3 &= (\mathbf{M} \cdot \mathbf{E})^3 - 3 (\mathbf{M} \cdot \mathbf{E}) (\mathbf{N} \cdot \mathbf{E})^2 = (E_R - E_\Theta)^3 \cos(6\phi), \end{aligned} \quad (4)$$

where  $\phi \in [0, \pi/6]$  and it represents the angle that principal direction 1 forms with zigzag direction (Fig. 2). Symmetry and periodicity of graphene allows us to investigate its material behavior in the domain between zigzag and armchair directions, inside which  $\phi = \Theta$ . Note that, in (4),  $I_1$  and  $I_2$  are the isotropic principal invariants of the Green-Lagrange strain tensor [29]. Anisotropy is introduced with the third invariant  $I_3$ , which plays a role only when deformations are relatively large and  $E_R \neq E_\Theta$ . Equation (4) is rewritten as a function of the principal stretches as follows:

$$\begin{aligned} I_1 &= \frac{1}{2} (\lambda_R^2 + \lambda_\Theta^2 - 2), \\ I_2 &= \frac{1}{4} (\lambda_R^2 - 1) (\lambda_\Theta^2 - 1), \\ I_3 &= \frac{1}{8} (\lambda_R^2 - \lambda_\Theta^2)^3 \cos(6\phi). \end{aligned} \quad (5)$$

In general, circular membranes composed of anisotropic materials lose their rotational symmetry when subjected to uniform lateral pressure. Nevertheless, this effect is negligible for the particular case of graphene

<sup>2</sup> Unit vectors  $\mathbf{n}_X$  and  $\mathbf{n}_Y$  identify respectively directions  $X$  and  $Y$  of the Cartesian coordinate system. Symbols  $\otimes$  and  $(\cdot)$  denote dyadic product and second-order tensor contraction, respectively.

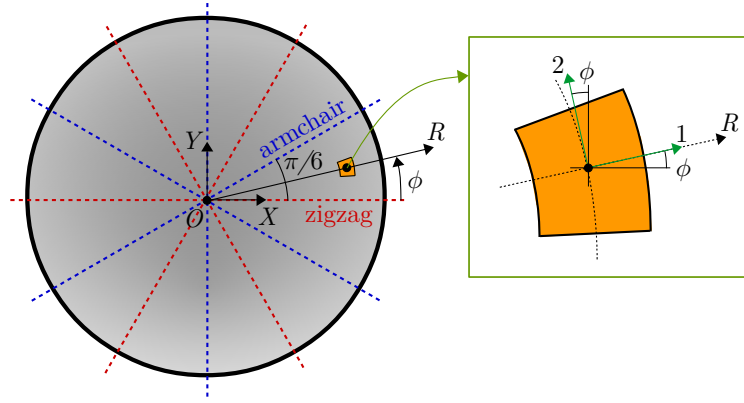


Fig. 2: Representation of the periodicity in the lattice structure of graphene, which repeats itself allowing to study its mechanical response within the domain identified by  $\phi \in [0, \pi/6]$ .

and the reason is as follows. As already pointed out, graphene breaks for deformations that are not very large. The ultimate value of strain is reached before that invariant  $I_3$  assumes a sensible importance. Specifically, term  $(\lambda_R^2 - \lambda_\Theta^2)^3$  is negligible with respect to the values assumed by the isotropic invariants  $I_1$  and  $I_2$ . Given the above, the hypothesis of axisymmetric kinematics of deformation is still valid and gives a simplified but effective description of the actual behavior of graphene. In any case, this assumption will be validated by the FE simulation, which will be presented in Section 3. It is worth saying that without this hypothesis on the kinematics it would be impossible to derive an analytical solution for the problem addressed in the present work. This clarifies the necessity and effectiveness of such assumption.

The most innovative and refined stored energy function for graphene was firstly introduced by Höller et al. [11] by fitting density functional theory (DFT) simulations. Subsequent works [28, 31] showed its validity and accuracy in the prediction of the graphene response subjected to large in-plane deformations. Therefore, we assume such hyperelastic material model for graphene. The stored energy function proposed in [11] is

$$\omega(I_1, I_2, I_3) = \frac{1}{t} \sum_{k=1}^3 c_k I_k + \frac{1}{t} \sum_{h=1}^{11} c_{h+3} J_h, \quad (6)$$

where  $c_1 - c_{14}$  are polynomial fitting coefficients with dimension of energy per unit area, whose values are reported in Tab. 3 of work [28]. Invariants  $J_h$  are defined as polynomial combinations of  $I_1$ ,  $I_2$  and  $I_3$  and their expressions are given in [11]. Being graphene a one-atom-thick layer, it is often treated as a two-dimensional material. In the expression of the stored energy function (6), we divided by thickness  $t$  so as to regard the graphene membrane as a three-dimensional solid and evaluate stress components with the usual dimension of force per unit area.

The second Piola-Kirchhoff stress tensor is energetically conjugated to the Green-Lagrange strain tensor and thus it is computed as

$$\Sigma = \frac{\partial \omega}{\partial \mathbf{E}}(I_1, I_2, I_3) = \sum_{k=1}^3 \frac{\partial \omega}{\partial I_k} \frac{\partial I_k}{\partial \mathbf{E}}, \quad (7)$$

where the derivatives of the principal invariants with respect to  $\mathbf{E}$  are

$$\frac{\partial I_1}{\partial \mathbf{E}} = \mathbf{n}_X \otimes \mathbf{n}_X + \mathbf{n}_Y \otimes \mathbf{n}_Y, \quad \frac{\partial I_2}{\partial \mathbf{E}} = I_1 (\mathbf{n}_X \otimes \mathbf{n}_X + \mathbf{n}_Y \otimes \mathbf{n}_Y) - \mathbf{E}, \quad \frac{\partial I_3}{\partial \mathbf{E}} = \mathbf{S},$$

with  $\mathbf{S} = 3 [(\mathbf{M} \cdot \mathbf{E})^2 - (\mathbf{N} \cdot \mathbf{E})^2] \mathbf{M} - 6 [(\mathbf{M} \cdot \mathbf{E})(\mathbf{N} \cdot \mathbf{E})] \mathbf{N}$ , whose representation in the cylindrical coordinate system is

$$[\mathbf{S}] = 3 (E_R - E_\Theta)^2 \begin{bmatrix} \cos(6\phi) & -\sin(6\phi) & 0 \\ -\sin(6\phi) & -\cos(6\phi) & 0 \\ 0 & 0 & 0 \end{bmatrix}.$$

We introduce invariants  $\beta_1$ ,  $\beta_2$  and  $\beta_3$ , defined as

$$\begin{aligned} \beta_1 &= c_1 + c_2 I_1 - 3c_5 I_2 + c_6 (I_1^2 + I_2) - 4c_7 I_1 I_2 + 2c_8 I_1 I_2 + c_9 (I_1^3 - 2I_1 I_2) \\ &\quad + 5c_{10} (I_2^2 - I_1^2 I_2) + c_{11} (I_1^4 - 3I_2^2 - 3I_1^2 I_2) + c_{12} (I_2^2 + 2I_1^2 I_2) + c_{13} I_3, \\ \beta_2 &= -c_2 + 2c_4 + 3c_5 I_1 - c_6 I_1 + 4c_7 (I_1^2 - I_2) - 2c_8 I_2 + c_9 (4I_2 - I_1^2) \\ &\quad + 5c_{10} (I_1^3 - 2I_1 I_2) + c_{11} (6I_1 I_2 - I_1^3) - 2c_{12} I_1 I_2 + 2c_{14} I_3, \\ \beta_3 &= c_3 + c_{13} I_1 + c_{14} (I_1^2 - 2I_2). \end{aligned} \quad (8)$$

From (7) we derive the following expressions for the components of the symmetric second Piola-Kirchhoff stress tensor:

$$\begin{aligned} \Sigma_{RR} &= \frac{\beta_1}{t} + \frac{\beta_2}{2t} (\lambda_R^2 - 1) + \frac{3\beta_3}{4t} (\lambda_R^2 - \lambda_\Theta^2)^2 \cos(6\phi), \\ \Sigma_{\Theta\Theta} &= \frac{\beta_1}{t} + \frac{\beta_2}{2t} (\lambda_\Theta^2 - 1) - \frac{3\beta_3}{4t} (\lambda_R^2 - \lambda_\Theta^2)^2 \cos(6\phi), \\ \Sigma_{R\Theta} &= -\frac{3\beta_3}{4t} (\lambda_R^2 - \lambda_\Theta^2)^2 \sin(6\phi), \\ \Sigma_{RZ} &= \Sigma_{\Theta Z} = \Sigma_{ZZ} = 0. \end{aligned} \quad (9)$$

It is assumed that the graphene undeformed configuration is stress free and therefore  $c_1 = 0$ .

Having at hand the second Piola-Kirchhoff stress tensor, the other stress measures can be derived. The first Piola-Kirchhoff stress tensor,  $\mathbf{T}_R = \mathbf{F}\mathbf{\Sigma}$ , reads

$$[\mathbf{T}_R] = \begin{bmatrix} \lambda_R \Sigma_{RR} \cos \psi & \lambda_R \Sigma_{R\Theta} \cos \psi & 0 \\ \lambda_\Theta \Sigma_{R\Theta} & \lambda_\Theta \Sigma_{\Theta\Theta} & 0 \\ -\lambda_R \Sigma_{RR} \sin \psi & -\lambda_R \Sigma_{R\Theta} \sin \psi & 0 \end{bmatrix}. \quad (10)$$

We immediately observe that, as required by the plane stress state, boundary conditions  $\pm \mathbf{T}_R \mathbf{n}_Z = \mathbf{0}$  are satisfied. This guarantees that the two external faces of the membrane are traction-free and all the stress components act in the plane of the deformed membrane.  $\mathbf{T}_R$  is not diagonal in reference system  $(R, \Theta, Z)$ , which is principal regarding the deformation. Hence, the principal strain directions do not coincide with the principal stress directions. This is not a surprise given that graphene is described by an anisotropic material model. In order to write the equilibrium in deformed configuration, we now derive the Cauchy stress tensor

134  $\mathbf{T} = \mathbf{T}_R \mathbf{F}^T / \det \mathbf{F}$ . By definition, tensor  $\mathbf{T}$  is symmetric and its components are

$$\begin{aligned} T_{RR} &= \frac{\lambda_R}{\lambda_\Theta} \Sigma_{RR} \cos^2 \psi, & T_{\Theta\Theta} &= \frac{\lambda_\Theta}{\lambda_R} \Sigma_{\Theta\Theta}, & T_{ZZ} &= \frac{\lambda_R}{\lambda_\Theta} \Sigma_{RR} \sin^2 \psi, \\ T_{R\Theta} &= \Sigma_{R\Theta} \cos \psi, & T_{RZ} &= -\frac{\lambda_R}{\lambda_\Theta} \Sigma_{RR} \cos \psi \sin \psi, & T_{\Theta Z} &= -\Sigma_{R\Theta} \sin \psi. \end{aligned} \quad (11)$$

135 At this point, the equilibrium allows us to derive a relationship between applied pressure and deflection  
 136 of the membrane. We adopted a semi-inverse approach, with which we set an appropriate kinematics of  
 137 deformation and accordingly we obtained the stress tensors. The kinematics of the model is not exact and thus  
 138 the local equilibrium equations can not be solved in every internal point of the membrane. The exact solution  
 139 to the local equilibrium can not be derived in closed-form and it would include a more general kinematics.  
 140 Nevertheless, we derive an analytical solution by imposing the equilibrium between applied pressure and  
 141 internal stresses in the neighborhood of the central point of the membrane, which is the most representative  
 142 point in this problem. With this aim, we firstly compute the Cauchy stress tensor for the limit case of  $R \rightarrow 0$ .  
 143 In this circumstance, radial and circumferential stretches correspond ( $\lambda_R = \lambda_\Theta|_{R \rightarrow 0} = \lambda$ ). Third invariant  $I_3$   
 144 goes to zero and the only non-zero components of the Cauchy stress tensor are

$$T_{RR}|_{R \rightarrow 0} = T_{\Theta\Theta}|_{R \rightarrow 0} = T_0 = \frac{1}{t} \beta_1|_{R \rightarrow 0} + \frac{1}{2t} \left( \psi_0^2 \csc \psi_0^2 - 1 \right) \beta_2|_{R \rightarrow 0}. \quad (12)$$

145 In the neighborhood of the central point, equilibrium along  $Z$  direction reads

$$p \left( \pi \rho^2 d\psi^2 \right) = T_0 (2\pi \rho d\psi t) d\psi,$$

146 from which we derive the following relationship between lateral pressure and kinematic parameter  $\rho$ :

$$p = \frac{2T_0 t}{\rho}. \quad (13)$$

147 Using (12), (8) and (5) and recalling that  $\rho = a/\sin \psi_0$ , equation (13) takes the form

$$p = \frac{1}{8a} \sin \psi_0 \sum_{j=1}^4 \kappa_j \left( \psi_0^2 \csc^2 \psi_0 - 1 \right)^j, \quad (14)$$

148 where

$$\kappa_1 = 8(c_2 + 2c_4), \quad \kappa_2 = 12(c_5 + c_6), \quad \kappa_3 = 4(2c_7 + c_8 + 2c_9), \quad \kappa_4 = 5(c_{10} + c_{11} + c_{12}).$$

149 Angle  $\psi_0$  is related to displacement  $\delta$  of the central node through  $\psi_0 = 2 \tan^{-1} \bar{\delta}$ , with  $\bar{\delta} = \delta/a$  denoting  
 150 the normalized deflection. By substitution into (14), the pressure-deflection relation for circular graphene  
 151 membranes is finally obtained.

## 2.1 Linear elastic constants of graphene

Graphene is isotropic when deformations are small. Hence, in linear elasticity its material behavior is entirely described by two constants: Young's modulus  $E$  and Poisson's ratio  $\nu$ . Expressions for  $E$  and  $\nu$  can be derived from the finite theory by introducing the hypothesis that both displacements and displacement gradients are small [4, 7]. To this aim, strain and stress measures are developed in Taylor series as functions of  $\psi_0$  and they are truncated at the second order. The Green-Lagrange strain tensor, expressed by (3), assumes the following linearized expression:

$$[\mathbf{E}] \cong \begin{bmatrix} \frac{\psi_0^2}{6} & 0 & 0 \\ 0 & \frac{(a-R)(a+R)\psi_0^2}{6a^2} & 0 \\ 0 & 0 & 0 \end{bmatrix}. \quad (15)$$

Tensor  $\mathbf{E}$  in linear elasticity is simply called strain tensor.

The linearization of the second Piola-Kirchhoff stress tensor  $\mathbf{\Sigma}$ , given by (9), provides

$$[\mathbf{\Sigma}] \cong \begin{bmatrix} \frac{\psi_0^2}{6t} \left[ \left( 1 - \frac{R^2}{a^2} \right) c_2 + 2c_4 \right] & 0 & 0 \\ 0 & \frac{\psi_0^2}{6t} \left[ c_2 + 2 \left( 1 - \frac{R^2}{a^2} \right) c_4 \right] & 0 \\ 0 & 0 & 0 \end{bmatrix}. \quad (16)$$

The development in Taylor series of both  $\mathbf{T}_R$  and  $\mathbf{T}$  (equations (11) and (10) respectively), with truncation at the second order in  $\psi_0$ , gives the same result as (16). Therefore, as it should be, in the linearized theory all the stress measures coincide and we may refer only to a single stress tensor, expressed by (16). Furthermore, we notice that the representation of the stress tensor in the principal strain system is diagonal. This indicates that in the linearized theory principal strain and stress directions coincide. This because graphene is isotropic for small deformations.

The Navier's constitutive relationships for plane stress are

$$\begin{aligned} \sigma_R &= \frac{E}{1-\nu^2} (\epsilon_R + \nu\epsilon_\Theta), \\ \sigma_\Theta &= \frac{E}{1-\nu^2} (\epsilon_\Theta + \nu\epsilon_R). \end{aligned} \quad (17)$$

Stress components  $\sigma_R$  and  $\sigma_\Theta$  are given respectively by the radial and circumferential components of the linearized stress tensor (16). Same goes for strain components  $\epsilon_R$  and  $\epsilon_\Theta$ , which are expressed by the strain tensor (15). Equation (17) transforms into the following linear system of two equations in the two unknown variables  $E$  and  $\nu$ :

$$\begin{aligned} \frac{8a^2c_4 + 4c_2(a-R)(a+R)}{t} + \frac{E[4a^2(\nu+1) - 4\nu R^2]}{\nu^2 - 1} &= 0, \\ \frac{4a^2c_2 + 8c_4(a-R)(a+R)}{t} + \frac{E[4a^2(\nu+1) - 4R^2]}{\nu^2 - 1} &= 0, \end{aligned}$$

whose solution gives the expressions of the elastic constants of graphene in linear elasticity

$$E = \frac{1}{t} \left( 2c_4 - \frac{c_2^2}{2c_4} \right), \quad \nu = \frac{c_2}{2c_4}. \quad (18)$$

This result corresponds to that derived by Höller et al. [11]. Under the hypothesis of homogeneous deformations, the authors obtained the expression of the tangent elasticity tensor. The linearization of such tensor with  $\mathbf{E} \rightarrow \mathbf{0}$  provided the Young's modulus and Poisson's ratio given in (18).

### 3 Finite element simulation

The FE model was realized by using software COMSOL Multiphysics version 6.0 [25]. The 3D membrane interface of the structural mechanics module was selected. This interface allows to model plane stress elements without bending stiffness that can deform both in the in-plane and out-of-plane directions.

The geometry of the membrane was defined through a work plane, in which a circle with radius  $a = 2.375 \mu\text{m}$  was built. This value of  $a$  is the one considered in the experimental and numerical investigations of works [13, 16, 40]. We will present comparisons of the results in the next section. The thickness of the membrane was set to  $t = 0.335 \text{ nm}$ . A fixed constraint was assigned along the perimeter. This reproduces the condition for which, along the constrained geometry, displacements are zero in all directions. A pressure load was applied to the free face of the membrane. The pressure load is a follower load, therefore its direction changes with deformation in the geometrically nonlinear analysis.

In the COMSOL membrane analysis it is necessary to apply a tensile prestress. This in order to avoid the singularity due to the fact that the undeformed membrane has no transverse stiffness. In our model, the prestress was introduced as an external in-plane force of  $0.001 \text{ N/m}$ , which is negligible compared to the stress values acting in the graphene membrane during the simulation. The sole scope of the prestress was to avoid the singularity and allow the solver to find a solution.

The material behavior was defined through the user-defined compressible hyperelastic material. In detail, the isotropic invariants were introduced as local variables according to (4). Anisotropy was added by subdividing the domain into subdomains. To do this, the membrane was cut by planes parallel to direction  $z$  and containing central point  $O$ . Starting from direction  $x$ , a plane was defined for every angle increment of 5 degrees (see Fig. 3a). The entire domain was thus partitioned into 72 subdomains. In each of them, invariant  $I_3$  was defined as a local variable with the corresponding value of  $\cos(6\phi)$ . In other words, the variation of term  $\cos(6\phi)$  in the expression of  $I_3$  was introduced in a discrete way by subdividing the membrane domain into several subdomains. It goes without saying that this is a simplification, but it gives a reasonable approximation of the continuous variation of  $I_3$  as a function of  $\phi$ . One may further subdivide the domain in order to reach more accuracy, but as we will see in the following the contribution of graphene anisotropy is negligible in the problem analyzed. The subdivision into 72 subdomains is already enough.

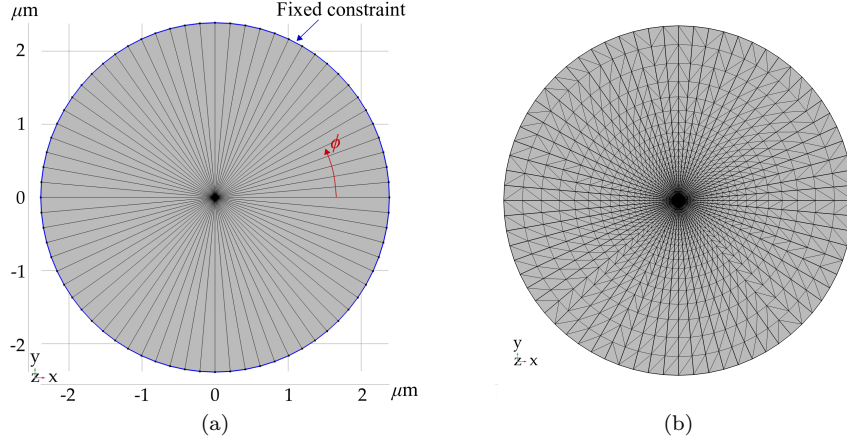


Fig. 3: FE simulation: (a) subdivided domain to define the anisotropic material properties of graphene and (b) mesh used for the analysis.

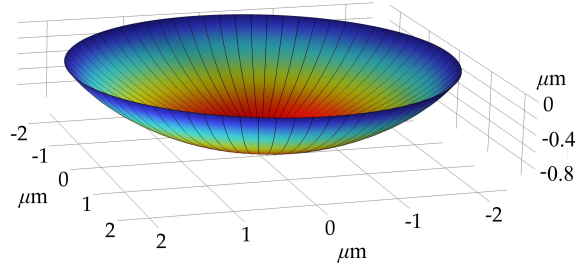


Fig. 4: Deformed configuration of the circular graphene membrane during the FE simulation.

The mesh was composed of triangular elements with minimum and maximum size of, respectively, 0.019 and 0.26  $\mu\text{m}$  (Fig. 3b). A stationary simulation was carried out and the applied pressure was increased from 5 Pa to 17 MPa. The stationary solver MUMPS was employed. The simulation stopped when a stationary value for the pressure was reached and thus, for further increasing values, convergence was not found anymore. Fig. 4 shows the deformed configuration of the circular graphene membrane for a certain value of applied pressure.

## 4 Results and comparison

In this section we put in comparison the results of the analytical model and the FE simulation. Note that in the FE software it is not possible to develop a 3D membrane model with no dependence on the transverse deformation. Therefore, the FE simulation takes into account the contraction of the membrane, which means that  $\lambda_z$  may assume values other than 1. This is in contrast with the assumption of the analytical model, according to which the graphene membrane can not undergo transverse contraction. Hence, to provide a consistent comparison, we derive the analytical solution by introducing  $\lambda_z$  in the equilibrium problem. The derivation of such solution is given in Appendix A. It is stressed that this solution has the sole scope of comparison with the FE simulation and thus validation of the model. The reference analytical solution remains



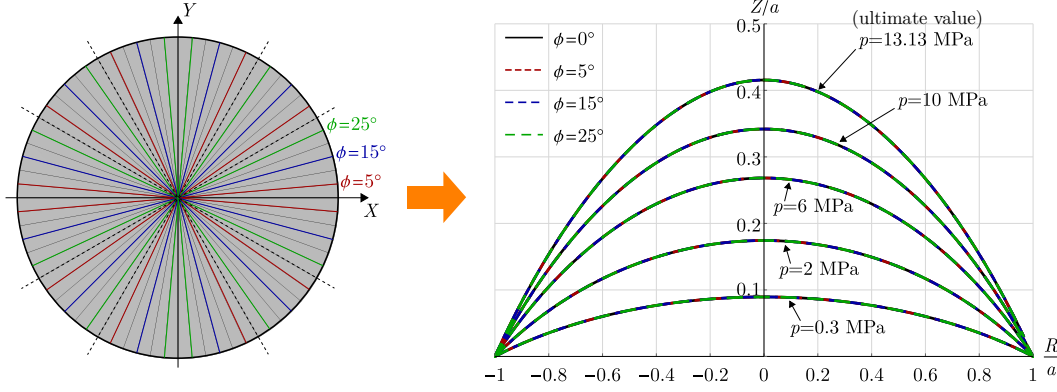


Fig. 5: Profiles of deformation from the FE simulation represented in the  $R$ - $Z$  plane and given in terms of dimensionless coordinates  $R/a$  and  $Z/a$  ( $a = 2.375 \mu\text{m}$ ). The deformed shapes along diameters with different angle  $\phi$  coincide and therefore the kinematics of deformation is axisymmetric.

the one derived in Section 2, which is more consistent with reality. After validating the model, a comparison with other results from experimental data and numerical simulations is presented.

#### 4.1 Validation of the model

The analytical model is based on the assumption that the kinematics of deformation maintains its rotational symmetry throughout the deformation process caused by the application of lateral pressure. This assumption is valid for isotropic materials, but in general not for anisotropic materials. However, due to the particular form of anisotropic invariant  $I_3$ , anisotropy of graphene plays a role only when deformations are large enough and the principal stretches do not coincide. For instance, anisotropy of graphene does not activate when it is subjected to equibiaxial loads.

In our problem, the difference between stretches  $\lambda_R$  and  $\lambda_\Theta$  is not large enough to activate anisotropy of graphene. This is demonstrated by Fig. 5, which shows the profiles of deformation along diameters of the membrane identified by different angles  $\phi$ . We observe that variations of  $\phi$  do not cause appreciable variations in the deformed shape, represented in the  $R$ - $Z$  plane. This means that the three-dimensional deformed configuration is axisymmetric with respect to  $Z$ . Further confirmation of this is given by Fig. 6a, which shows normalized displacement  $u_Z/a$  in the  $X$ - $Y$  plane for the ultimate value of pressure computed during the FE simulation. It is clearly visible that  $u_Z$  is axisymmetric. In addition, Fig. 6b shows the trend of invariant  $I_3$  in the membrane domain. Its values are very close to zero in the entire domain, except from the areas close to the perimeter. This because in such areas, due to the influence of the constrained boundary, stretches  $\lambda_R$  and  $\lambda_\Theta$  differ more than in the inner region. Nevertheless, the values assumed by  $I_3$  are largely negligible with respect to the other deformation quantities and therefore anisotropy of graphene does not play a noticeable role. The above discussion demonstrates that the assumption of rotational symmetry in the analytical model is accurate and in accordance with the FE simulation.

We now focus on the comparison of the pressure-deflection curves, which is reported in Fig. 7. Both analytical models with and without transverse contraction are represented. The accuracy of the analytical

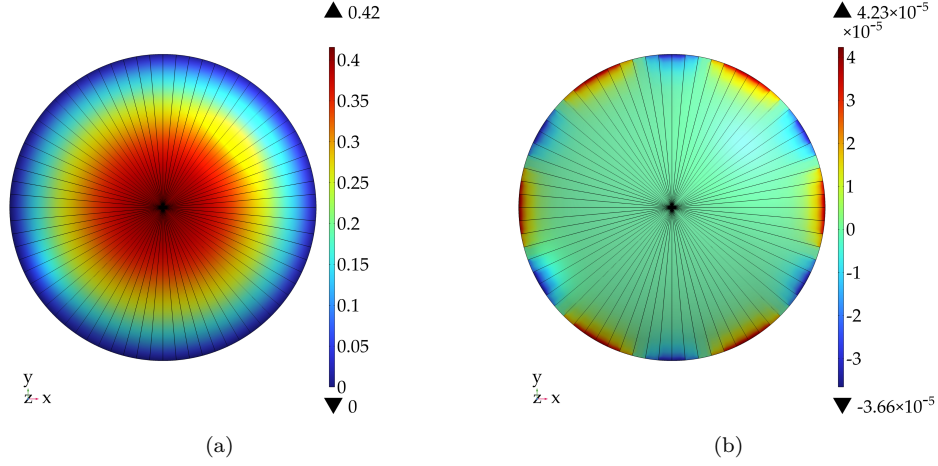


Fig. 6: (a) Normalized deflection  $u_z/a$  and (b) invariant  $I_3$  at the ultimate value of pressure from the FE simulation. The values of  $I_3$  are negligible and thus anisotropy of graphene does not activate.

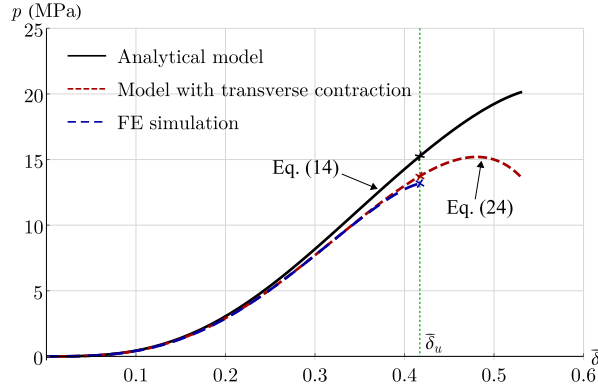


Fig. 7: Pressure-deflection curves with  $\bar{\delta} = \delta/a$  of a circular graphene sheet with radius  $2.375 \mu\text{m}$ . Black and red curves represent respectively the analytical models with and without transverse contraction, while the blue curve is the FE simulation.

model is demonstrated by the good agreement between FE simulation and analytical model with transverse contraction, expressed by Eq. (14). The two pressure-deflection curves match until  $\bar{\delta}$  assumes values greater than 0.4. Afterwards, the curve from the FE model is less stiff and the simulation ended as soon as the stationary value of pressure was reached. This discrepancy is explained by observing the comparison of the deformation profiles given in Fig. 8. The analytical and FE deformed configurations almost coincide for  $\bar{\delta} \leq 0.4$ , but then the membrane in the FE model experienced a higher deformation concentrated in the area close to the center. This produced a reduction of the stiffness and a rapid attainment of the ultimate value of pressure  $p_u = 13.13 \text{ MPa}$ . The ultimate value of stretch at the pole in the FE simulation is  $\lambda_u = 1.17$ , which corresponds to the ultimate normalized displacement  $\bar{\delta}_u = 0.42$ .

In light of the above considerations, the analytical model proposed in this work can be considered very accurate. The hypothesis on the kinematics of deformation generates some discrepancies in the pressure-deflection curve only when the system is close to the ultimate configuration. The value of pressure at  $\bar{\delta}_u$  predicted by the model is  $13.67 \text{ MPa}$  and the relative error with respect to the FE prediction is 4%, which is

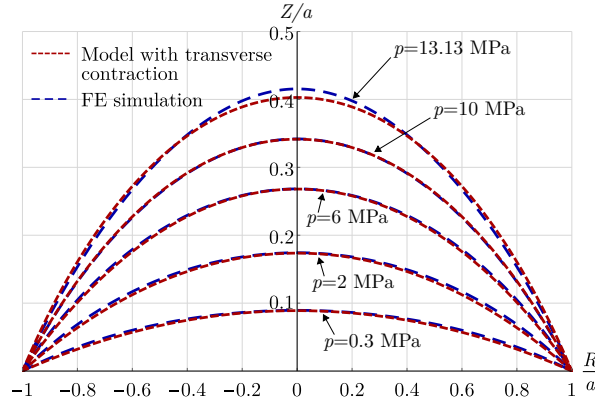


Fig. 8: Profiles of deformation from analytical model (with transverse contraction) and FE simulation represented in the  $R$ - $Z$  plane and given in terms of dimensionless coordinates  $R/a$  and  $Z/a$ .

largely acceptable. The analytical model should be applied by assuming as ultimate displacement  $\bar{\delta}_u = 0.42$ , which comes from the FE prediction.

We recall that the model with transverse contraction described in Appendix A was introduced with the sole purpose of comparison with the FE simulation and consequent validation. As already pointed out, the model that is most consistent with the real response of graphene is the one without transverse contraction, expressed by relation (14). The pressure-deflection curve given by such model is depicted in Fig. 7. As expected, the fact that graphene can not deform along its thickness makes its response sensibly stiffer, especially when deformations become moderately large. Indeed, the ultimate pressure value is 15.16 MPa, with an increment of 15% with respect to the FE prediction, which includes transverse contraction of the membrane. In light of this, FE simulations of graphene subjected to large deformations should be carried out carefully, reminding that the response might be sensibly underestimated.

In the following we present a comparison with other results from the literature. In light of the above discussion, from now on the reference analytical model is the one without transverse contraction.

#### 4.2 Comparison with other results

The results are now put in comparison with other models, numerical simulations and experiments found in the literature. The well-known Fitcher's model [6] is considered and, for the sake of brevity, it is outlined in Appendix B. The experimental data that we consider are reported in the work by Koenig et al. [16]. In that work, the authors produced monolayer graphene sheets through mechanical exfoliation over predefined microcavities etched in a silica substrate. The microcavities had diameter of around  $4.75 \mu\text{m}$ . A bulge test was performed using a pressure chamber and the deformed shape of the graphene membrane was measured with an atomic force microscope. For the comparison we also consider the FE simulation carried out by Jiang et al. [13]. The FE model was built in software COMSOL Multiphysics using a plate element composed of linearly elastic and isotropic material. The circular plate had diameter of  $4.75 \mu\text{m}$  and it was clamped along the boundary. Geometric nonlinearity was included in the solution.

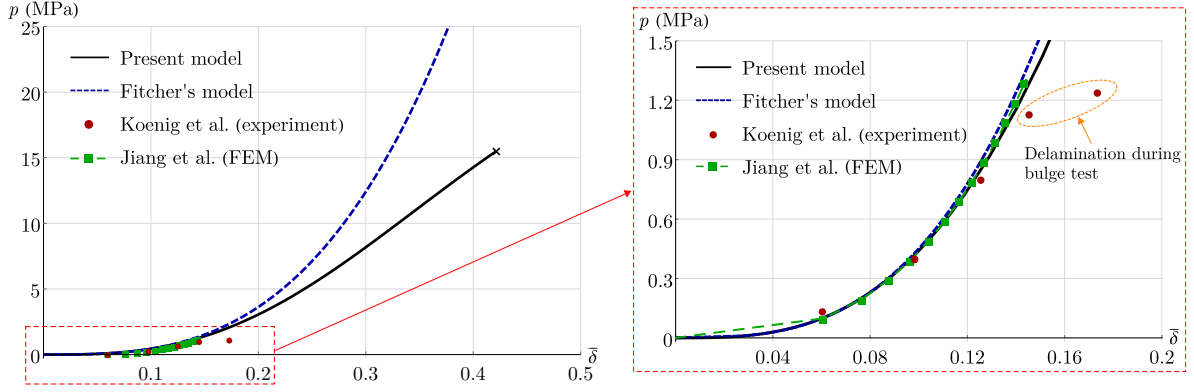


Fig. 9: Comparison of the pressure-deflection curves obtained with the proposed model, Fitcher's model [6], experiment from Koenig et al. [16] and FE simulation carried out by Jiang et al. [13] for a graphene membrane with diameter  $4.75 \mu\text{m}$ .

Figure 9 shows the comparison of the pressure-deflection curves. The black curve (present model) is expressed by equation (14). The Fitcher's solution is in good agreement with our model only for small values of  $\bar{\delta}$ . This is because Fitcher's model is based on the assumption of linear elastic material. Such assumption is not suitable for graphene, which exhibits material nonlinearity even for relatively small values of strain [10, 23]. In particular, the uniaxial stress-strain response of graphene shows a progressive reduction of its stiffness until the attainment of the ultimate stress. This is not taken into account in Fitcher's model and the result is that, as the strain increases, the gap between its prediction and our model increases. Fitcher's model is always stiffer because it does not include the stiffness reduction of graphene due to nonlinearity.

From the right side of Fig. 9 we observe a good agreement of our model with the experimental data by Koenig et al. [16]. However, at some point of the experiment a delamination of graphene from the silica substrate took place. This explains why the last two experimental data (red dots) deviate from the analytical prediction. Very good agreement is found also with the FE simulation of Jiang et al. [13]. Note that their simulation was based on the assumption of linear elastic material. In fact, when  $\bar{\delta}$  exceeds 0.12 their prediction becomes slightly stiffer than the response of our model.

Further comparisons are presented in Fig. 10. In particular, in Fig. 10a we consider the FE simulation carried out by Wang et al. [40] using software ANSYS. The authors used 2-node axisymmetric shell elements composed of a linear elastic material with  $E = 1 \text{ TPa}$  and  $\nu = 0.17$ . As expected, for the same reasons explained previously, the FE simulation matches well with our model only for relatively small deflections. It is demonstrated once again that the material nonlinearity of graphene plays an important role and must be considered.

Fig. 10b shows a comparison with the molecular dynamics (MD) simulation carried out by Wang et al. [42], which is displayed in green color. The graphene membrane had diameter 10 nm. The choice of such a small diameter is due to the fact that MD simulations require a large computational effort and therefore they can be applied only to systems with a relatively small number of atoms. Although the computational strategy is different from the continuum modeling, the simulation is in good agreement with the present

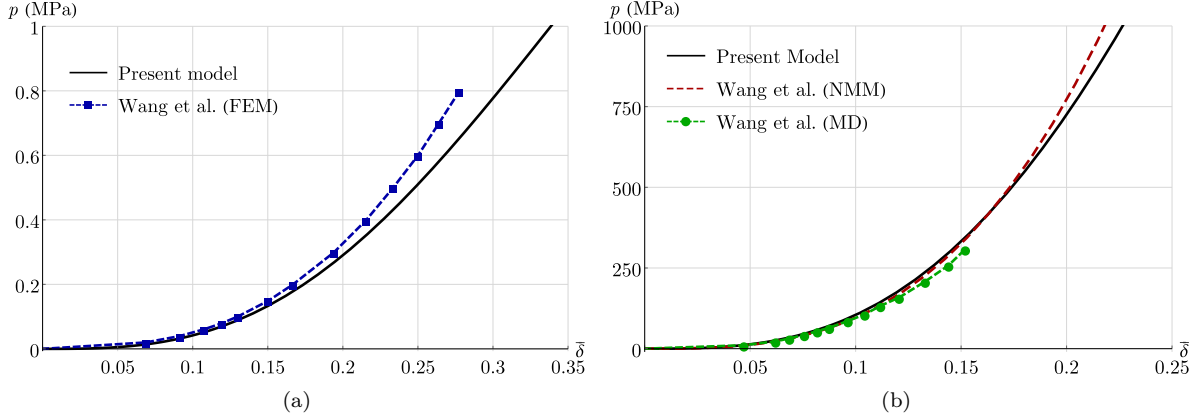


Fig. 10: Comparison with (a) FE simulation of a graphene sheet with diameter  $50 \mu\text{m}$ , reported in Wang et al. [40], and (b) nonlinear membrane model (NMM) and molecular dynamics (MD) simulation of a graphene sheet with diameter  $10 \text{ nm}$ , reported in Wang et al. [42].

model. The gap is mainly due to the parametrization of the interatomic potential describing the carbon-carbon interactions in graphene. Wang et al. [42] adopted the second-generation reactive empirical bond-order (REBO-2) potential [1], but there are several potentials that can be used and may lead to sensibly different results [8, 9, 26]. The coefficients of the stored energy function (6) adopted in this work were estimated by fitting molecular mechanics simulations based on the modified Morse potential [28], which is considered the most reliable for describing the carbon-carbon interactions in graphene.

A nonlinear membrane model (NMM) was also proposed by Wang et al. [42] (equations (3.4) and (3.5) in [42]). The corresponding response of the pressurized graphene membrane is depicted in Fig. 10b. We observe again a good match with our analytical prediction for relatively small deflections. The model proposed in [42] does not take into account material nonlinearity and thus it deviates from our model as the deflection increases.

## 5 Conclusions

In the present work we analyzed the problem of circular graphene membranes subjected to uniform lateral pressure. The analytical formulation was developed in finite elasticity, considering both material and geometric nonlinearities. The kinematics of deformation was described by assuming that the membrane preserves the axisymmetry and deforms into a spherical cap. Such assumptions are accurate up to moderately large strains and therefore are suitable to describe the behavior of graphene, which reaches failure for uniaxial elongations of around 15-20%.

The material behavior was described by a hyperelastic stored energy function that takes into account both nonlinearity and anisotropy of graphene. The isotropicization theorem allowed us to derive the Piola-Kirchhoff and Cauchy stress tensors. The equilibrium for  $R \rightarrow 0$  was written and an expression of the applied pressure as a function of the deflection of the membrane was derived.

A FE model was built in software COMSOL Multiphysics using the 3D membrane interface. Both material nonlinearity and anisotropy of graphene were included. It was shown that for circular pressurized graphene

membranes the effect of material anisotropy is negligible and thus the deformed configuration remains axisymmetric. Furthermore, it was demonstrated that a spherical cap provides an accurate description of the kinematics of deformation. The hypotheses of the analytical formulation proposed in this work were thus validated. The results of the simulation were in good agreement with the prediction of the analytical model.

We presented a comparison with other models, numerical simulations and experiments found in the literature. Good agreement in the pressure-deflection curves was found only for relatively small deflections. This because, differently from our entirely nonlinear approach, all the continuum models in the literature are based on the assumption of linear elastic material. This emphasizes the novelty of the present work and the advantages of the proposed model.

The model is an effective and useful tool for an accurate prediction of the response of pressurized graphene membranes. For the first time, a pressure-deflection relation in nonlinear elasticity was proposed. This is a great advantage in terms of applicability because it does not require any computational effort, which is the main concern in atomistic and FE simulations. Moreover, it is not easy to define the nonlinear material behavior of graphene in FE models. In addition, FE models in finite elasticity include transverse contraction, which is not present in the real behavior of a single layer graphene sheet. It was shown that this leads to an underestimation of the response of the membrane, especially when deformations become relatively large.

### Acknowledgments

This work was supported by the Italian Ministry of University and Research (MUR) through research grant PRIN 2020 No. 2020EBLPLS on “Opportunities and challenges of nanotechnology in advanced and green construction materials” and through project FISR 2019: “Eco Earth” (code 00245). Financial support by the National Group of Mathematical Physics (GNFM-INdAM) is also acknowledged.

### Compliance with Ethical Standards

Conflict of Interest: The authors declare that they have no conflict of interest.

### A Analytical solution with transverse contraction

After deformation, thickness  $t$  transforms into  $t' = \lambda_Z t$ . This transverse contraction is introduced by defining the deformation gradient as follows:

$$[\mathbf{F}] = \begin{bmatrix} \rho \frac{\partial \psi}{\partial R} \cos \psi & 0 & \lambda_Z \sin \psi \\ 0 & \frac{\rho \sin \psi}{R} & 0 \\ -\rho \frac{\partial \psi}{\partial R} \sin \psi & 0 & \lambda_Z \cos \psi \end{bmatrix}.$$

353 Rotation tensor  $\mathbf{R}$  remains unchanged and pure deformation tensor  $\mathbf{U}$  becomes

$$[\mathbf{U}] = \begin{bmatrix} \rho \frac{\partial \psi}{\partial R} & 0 & 0 \\ 0 & \frac{\rho \sin \psi}{R} & 0 \\ 0 & 0 & \lambda_Z \end{bmatrix}.$$

354 The right Cauchy-Green deformation tensor and the Green-Lagrange strain tensor expressed in cylindrical coordinates  
355 assume the form

$$[\mathbf{C}] = \begin{bmatrix} \lambda_R^2 & 0 & 0 \\ 0 & \lambda_\Theta^2 & 0 \\ 0 & 0 & \lambda_Z^2 \end{bmatrix}, \quad [\mathbf{E}] = \frac{1}{2} \begin{bmatrix} \lambda_R^2 - 1 & 0 & 0 \\ 0 & \lambda_\Theta^2 - 1 & 0 \\ 0 & 0 & \lambda_Z^2 - 1 \end{bmatrix},$$

356 where  $\lambda_R$  and  $\lambda_\Theta$  are given by (2).

357 Strain invariants  $I_1$  and  $I_2$  become

$$\begin{aligned} I_1 &= \frac{1}{2} (\lambda_R^2 + \lambda_\Theta^2 + \lambda_Z^2 - 3), \\ I_2 &= \frac{1}{4} (\lambda_R^2 - 1) (\lambda_\Theta^2 - 1) + \frac{1}{4} (\lambda_R^2 - 1) (\lambda_Z^2 - 1) + \frac{1}{4} (\lambda_\Theta^2 - 1) (\lambda_Z^2 - 1), \end{aligned} \quad (19)$$

358 while invariant  $I_3$  has the same expression as in (5). The second Piola-Kirchhoff stress tensor is computed using (7),  
359 obtaining

$$\begin{aligned} \Sigma_{RR} &= \frac{\beta_1}{t} + \frac{\beta_2}{2t} (\lambda_R^2 - 1) + \frac{3\beta_3}{4t} (\lambda_R^2 - \lambda_\Theta^2)^2 \cos(6\phi), \\ \Sigma_{\Theta\Theta} &= \frac{\beta_1}{t} + \frac{\beta_2}{2t} (\lambda_\Theta^2 - 1) - \frac{3\beta_3}{4t} (\lambda_R^2 - \lambda_\Theta^2)^2 \cos(6\phi), \\ \Sigma_{ZZ} &= \frac{\beta_1}{t} + \frac{\beta_2}{2t} (\lambda_Z^2 - 1), \\ \Sigma_{R\Theta} &= -\frac{3\beta_3}{4t} (\lambda_R^2 - \lambda_\Theta^2)^2 \sin(6\phi), \quad \Sigma_{RZ} = \Sigma_{\Theta Z} = 0, \end{aligned} \quad (20)$$

360 where  $\beta_1$ ,  $\beta_2$  and  $\beta_3$  are given in (8). The first Piola-Kirchhoff stress tensor is thus derived

$$[\mathbf{T}_R] = \begin{bmatrix} \lambda_R \Sigma_{RR} \cos \psi & \lambda_R \Sigma_{R\Theta} \cos \psi & \lambda_Z \Sigma_{ZZ} \sin \psi \\ \lambda_\Theta \Sigma_{R\Theta} & \lambda_\Theta \Sigma_{\Theta\Theta} & 0 \\ -\lambda_R \Sigma_{RR} \sin \psi & -\lambda_R \Sigma_{R\Theta} \sin \psi & \lambda_Z \Sigma_{ZZ} \cos \psi \end{bmatrix}.$$

361 Boundary conditions  $\pm \mathbf{T}_R \mathbf{n}_Z = \mathbf{0}$  require that

$$\lambda_Z \Sigma_{ZZ} \sin \psi = 0 \quad \text{and} \quad \lambda_Z \Sigma_{ZZ} \cos \psi = 0, \quad \forall \psi \in [0, \pi/6], \quad (21)$$

362 which are satisfied only if  $\Sigma_{ZZ} = 0$ . From this condition and recalling (20), we derive the following implicit expression of  
363 stretch  $\lambda_Z$ :

$$\lambda_Z = \sqrt{1 - 2 \frac{\beta_1}{\beta_2}}. \quad (22)$$

364 Finally, the components of the Cauchy stress tensor read

$$\begin{aligned} T_{RR} &= \frac{\lambda_R}{\lambda_\Theta \lambda_Z} \Sigma_{RR} \cos^2 \psi, & T_{\Theta\Theta} &= \frac{\lambda_\Theta}{\lambda_R \lambda_Z} \Sigma_{\Theta\Theta}, & T_{ZZ} &= \frac{\lambda_R}{\lambda_\Theta \lambda_Z} \Sigma_{RR} \sin^2 \psi, \\ T_{R\Theta} &= \frac{1}{\lambda_Z} \Sigma_{R\Theta} \cos \psi, & T_{RZ} &= -\frac{\lambda_R}{\lambda_\Theta \lambda_Z} \Sigma_{RR} \cos \psi \sin \psi, & T_{\Theta Z} &= -\frac{1}{\lambda_Z} \Sigma_{R\Theta} \sin \psi, \end{aligned}$$

365 with  $\lambda_Z$  expressed by (22).

366 As we did in Section 2, we now write the equilibrium in the neighborhood of the central point of the membrane. With  
367 this aim, we firstly compute the Cauchy stress tensor for the limit case of  $R \rightarrow 0$ . Radial and circumferential stretches  
368 correspond ( $\lambda_R = \lambda_\Theta|_{R \rightarrow 0} = \lambda$ ) and third invariant  $I_3$  goes to zero. The only non-zero components of the Cauchy stress

369 tensor are

$$T_{RR}|_{R \rightarrow 0} = T_{\Theta\Theta}|_{R \rightarrow 0} = T_0 = \frac{\psi_0^2 \csc \psi_0^2 - \lambda_Z^2|_{R \rightarrow 0}}{2t \lambda_Z|_{R \rightarrow 0}} \beta_2|_{R \rightarrow 0}. \quad (23)$$

370 Hereinafter, for the sake of simplicity, we indicate  $\lambda_Z|_{R \rightarrow 0}$  simply with  $\lambda_Z$ . Equilibrium equation (13) becomes

$$p = \frac{2T_0 \lambda_Z t}{\rho},$$

371 from which, using (23), (8) and (19), we derive the following expression of the applied pressure:

$$p = \frac{\sin \psi_0}{8a} \left( \psi_0^2 \csc^2 \psi_0 - \lambda_Z^2 \right) \sum_{j=0}^3 \zeta_j \psi_0^{2j} \csc^{2j} \psi_0, \quad (24)$$

372 where

$$\begin{aligned} \zeta_0 &= \lambda_Z^2 \left[ \lambda_Z^2 \left( 5c_{10} \lambda_Z^2 - c_{11} \lambda_Z^2 - 25c_{10} - 3c_{11} + 4c_{12} \right) + 8c_7 \left( \lambda_Z^2 - 4 \right) - 2c_9 \left( \lambda_Z^2 + 2 \right) - 4c_6 + 8c_8 + 9 \left( 5c_{10} + 3c_{11} - 2c_{12} \right) \right] \\ &\quad + 12c_5 \left( \lambda_Z^2 - 3 \right) - 8c_2 + 16c_4 + 3 \left( 4c_6 + 16c_7 - 4c_8 + 2c_9 - 15c_{10} - 9c_{11} + 6c_{12} \right), \\ \zeta_1 &= 2\lambda_Z^2 \left[ 3c_{11} \left( \lambda_Z^2 - 8 \right) - 2c_{12} \left( \lambda_Z^2 - 7 \right) + 5c_{10} \left( \lambda_Z^2 - 4 \right) - 4c_8 + 4c_9 \right] + 16c_7 \left( \lambda_Z^2 - 4 \right) \\ &\quad + 24c_5 - 8c_6 + 16c_8 - 8c_9 + 90c_{10} + 54c_{11} - 36c_{12}, \\ \zeta_2 &= 2 \left[ c_{12} \left( 11 - 5\lambda_Z^2 \right) + 5c_{10} \left( \lambda_Z^2 - 7 \right) + 3c_{11} \left( 3\lambda_Z^2 - 5 \right) + 12c_7 - 2c_8 \right], \\ \zeta_3 &= 4 \left( 5c_{10} + c_{11} - c_{12} \right). \end{aligned}$$

373 An explicit expression of stretch  $\lambda_Z$  is derived by satisfying condition (21) for the limit case of  $R \rightarrow 0$ , for which  $\lambda_R =$   
374  $\lambda_{\Theta}|_{R \rightarrow 0} = \lambda$ . In this case, substitution of (8) and (19) into (22) gives

$$\sqrt{\eta} - \sqrt{\frac{\Delta_n}{\Delta_d}} = 0, \quad (25)$$

375 with  $\eta = \lambda_Z^2$  and

$$\begin{aligned} \Delta_n &= -8c_2 \left( \eta + 2\lambda^2 - 2 \right) + 16c_4 + 12c_5 \left[ -\eta + 2 \left( \eta - 1 \right) \lambda^2 + \lambda^4 \right] - 4c_6 \left[ \eta^2 - 7\eta + 2 \left( 3\eta - 7 \right) \lambda^2 + 5\lambda^4 + 9 \right] \\ &\quad + 8c_7 \left[ -\eta^2 + 5\eta + \left( 5\eta - 8 \right) \lambda^4 + 2 \left( \eta - 5 \right) \left( \eta - 1 \right) \lambda^2 + 2\lambda^6 - 3 \right] - 4c_8 \left( \lambda - 1 \right) \left( \lambda + 1 \right) \left( 2\eta + \lambda^2 - 3 \right) \left( \eta + 2\lambda^2 - 2 \right) \\ &\quad - 2c_9 \left[ \eta^3 - 4\eta^2 + 11\eta + 2 \left( \eta - 7 \right) \lambda^4 + 2 \left( \eta^2 - 6\eta + 11 \right) \lambda^2 + 4\lambda^6 - 12 \right] \\ &\quad + 5c_{10} \left\{ -\eta^3 + 6\eta^2 - 15\eta + 8 \left( \eta - 2 \right) \lambda^6 + \left[ \eta \left( 5\eta - 32 \right) + 33 \right] \lambda^4 + 2 \left( \eta - 1 \right) \left[ \left( \eta - 6 \right) \eta + 15 \right] \lambda^2 + 3\lambda^8 + 9 \right\} \\ &\quad - c_{11} \left\{ \eta \left[ \left( \eta - 5 \right) \eta^2 + 9 \right] + 8 \left( 1 - 2\eta \right) \lambda^6 - 3 \left[ 5 \left( \eta - 4 \right) \eta + 9 \right] \lambda^4 + 2 \left[ \eta \left( \eta^2 + 9\eta - 27 \right) + 9 \right] \lambda^2 + \lambda^8 \right\} \\ &\quad - c_{12} \left( \lambda - 1 \right) \left( \lambda + 1 \right) \left( 2\eta + \lambda^2 - 3 \right) \left[ 2 \left( \eta - 6 \right) \eta + 10\eta\lambda^2 + 9\lambda^4 - 24\lambda^2 + 15 \right], \\ \Delta_d &= -8c_2 + 16c_4 + 12c_5 \left( \eta + 2\lambda^2 - 3 \right) - 4c_6 \left( \eta + 2\lambda^2 - 3 \right) + 8c_7 \left[ \eta^2 + 2 \left( \eta - 4 \right) \lambda^2 - 4\eta + 3\lambda^4 + 6 \right] \\ &\quad - 4c_8 \left( \lambda^2 - 1 \right) \left( 2\eta + \lambda^2 - 3 \right) - 2c_9 \left( \eta - 1 \right) \left( \eta - 4\lambda^2 + 3 \right) + 5c_{10} \left( \eta + 2\lambda^2 - 3 \right) \left[ \left( \eta - 2 \right) \eta + 2\lambda^4 - 4\lambda^2 + 3 \right] \\ &\quad - c_{11} \left( \eta + 2\lambda^2 - 3 \right) \left[ \eta^2 + 4 \left( 3 - 2\eta \right) \lambda^2 + 6\eta - 2\lambda^4 - 9 \right] - 2c_{12} \left( \lambda - 1 \right) \left( \lambda + 1 \right) \left( 2\eta + \lambda^2 - 3 \right) \left( \eta + 2\lambda^2 - 3 \right). \end{aligned}$$

376 Equation (25) admits four solutions in  $\eta$ . Two solutions are not real and another one does not respect condition  $\eta = 1$   
377 when  $\lambda = 1$ . The remaining solution is the correct one. We do not report this solution due to its very long mathematical  
378 expression. Having obtained an explicit expression for  $\eta$ , we compute  $\lambda_Z = \sqrt{\eta}$  and by substitution into (24) we finally  
379 derive the pressure-deflection equation. We recall that relation  $\psi_0 = 2 \tan^{-1} \bar{\delta}$  allows us to obtain a direct expression of  
380 pressure as a function of deflection.



## B Fitcher's model

Fitcher's model is based on the assumption that the material is linearly elastic. In this case, the equilibrium equations are

$$\begin{aligned} N^2 \left( \bar{R}^2 \frac{d^2 N}{d\bar{R}^2} + 3\bar{R} \frac{dN}{d\bar{R}} \right) - \frac{1}{2} \bar{R}^3 \frac{dN}{d\bar{R}} + \frac{1}{2} (3 + \nu) \bar{R}^2 N + \frac{1}{4} \frac{\bar{R}^2 E H}{pL} &= 0, \\ N \frac{d\bar{\delta}}{d\bar{R}} + \frac{1}{2} \bar{R} &= 0, \end{aligned} \quad (26)$$

where  $\bar{R} = R/a$ ,  $E$  is the Young's modulus,  $\nu$  is the Poisson's ratio and  $N = N_R/(pa)$ , with  $N_R$  indicating the radial stress resultant. Young's modulus and Poisson's ratio of graphene are computed using (18), obtaining  $E = 1042.9$  GPa and  $\nu = 0.146$ . The solution for both stress resultant and deflection is found in the form of a power series

$$\begin{aligned} N(\bar{R}) &= \sum_{m=0}^{\infty} n_{2m} \bar{R}^{2m}, \\ \bar{\delta}(\bar{R}) &= \sum_{n=0}^{\infty} w_{2n} (1 - \bar{R}^{2n+2}). \end{aligned} \quad (27)$$

Substituting (27)<sub>1</sub> into (26)<sub>1</sub> and equating coefficients of like powers of  $\bar{R}$  we obtain a system of equations that allows to derive the expressions of coefficients  $n_{2m}$  as functions of  $n_0$ . Likewise, substituting (27)<sub>2</sub> into (26)<sub>2</sub> and equating coefficients of like powers of  $\bar{R}$  we derive the expressions of coefficients  $w_{2n}$  as functions of  $n_0$ . Finally,  $n_0$  is evaluated by imposing the following boundary condition on radial displacement:

$$\left\{ \bar{R} \left[ \frac{d}{d\bar{R}} (\bar{R}N) - \nu N - \bar{R} \frac{d\bar{\delta}}{d\bar{R}} \right] \right\} \bigg|_{\bar{R}=1} = 0.$$

This procedure was implemented in software Wolfram Mathematica. A vector of increasing pressure values was defined and, for each value, the solution was obtained by considering twelve terms in the power series ( $m = 12$  and  $n = 12$ ). More terms did not cause sensible variations in the solutions and only increased the computational burden.

## References

- Brenner, D.W., Shenderova, O.A., Harrison, J.A., Stuart, S.J., Ni, B., Sinnott, S.B.: A second-generation reactive empirical bond order (REBO) potential energy expression for hydrocarbons. *Journal of Physics: Condensed Matter* **14**(4), 783 (2002)
- Bunch, J.S., Verbridge, S.S., Alden, J.S., Van Der Zande, A.M., Parpia, J.M., Craighead, H.G., McEuen, P.L.: Impermeable atomic membranes from graphene sheets. *Nano letters* **8**(8), 2458–2462 (2008)
- Caillerie, D., Mourad, A., Raoult, A.: Discrete homogenization in graphene sheet modeling. *Journal of Elasticity* **84**(1), 33–68 (2006)
- Casey, J.: On infinitesimal deformation measures. *Journal of Elasticity* **28**(3), 257–269 (1992)
- Fang, M., Wang, K., Lu, H., Yang, Y., Nutt, S.: Covalent polymer functionalization of graphene nanosheets and mechanical properties of composites. *Journal of Materials Chemistry* **19**(38), 7098–7105 (2009)
- Fichter, W.B.: Some solutions for the large deflections of uniformly loaded circular membranes, vol. 3658. National Aeronautics and Space Administration, Langley Research Center (1997)
- Freddi, F., Royer-Carfagni, G.: From non-linear elasticity to linearized theory: examples defying intuition. *Journal of Elasticity* **96**(1), 1–26 (2009)
- Genoese, A., Genoese, A., Rizzi, N.L., Salerno, G.: On the derivation of the elastic properties of lattice nanostructures: the case of graphene sheets. *Composites Part B: Engineering* **115**, 316–329 (2017)
- Genoese, A., Genoese, A., Salerno, G.: In-plane and out-of-plane tensile behaviour of single-layer graphene sheets: a new interatomic potential. *Acta Mechanica* **231**(7), 2915–2930 (2020)
- Georgantzinos, S.K., Katsareas, D.E., Anifantis, N.K.: Graphene characterization: A fully non-linear spring-based finite element prediction. *Physica E: Low-dimensional Systems and Nanostructures* **43**(10), 1833–1839 (2011)
- Höller, R., Smejkal, V., Libisch, F., Hellmich, C.: Energy landscapes of graphene under general deformations: DFT-to-hyperelasticity upscaling. *International Journal of Engineering Science* **154**, 103342 (2020)
- Hossain, M.Z., Ahmed, T., Silverman, B., Khawaja, M.S., Calderon, J., Rutten, A., Tse, S.: Anisotropic toughness and strength in graphene and its atomistic origin. *Journal of the Mechanics and Physics of Solids* **110**, 118–136 (2018)
- Jiang, S., Shi, S., Wang, X.: Nanomechanics and vibration analysis of graphene sheets via a 2D plate model. *Journal of Physics D: Applied Physics* **47**(4), 045104 (2013)
- Kang, X., Wang, J., Wu, H., Liu, J., Aksay, I.A., Lin, Y.: A graphene-based electrochemical sensor for sensitive detection of paracetamol. *Talanta* **81**(3), 754–759 (2010)
- Kausar, A.: Applications of polymer/graphene nanocomposite membranes: a review. *Materials Research Innovations* **23**(5), 276–287 (2019)

16. Koenig, S.P., Boddeti, N.G., Dunn, M.L., Bunch, J.S.: Ultrastrong adhesion of graphene membranes. *Nature nanotechnology* **6**(9), 543–546 (2011)
17. Korobeynikov, S.N., Alyokhin, V.V., Babichev, A.V.: On the molecular mechanics of single layer graphene sheets. *International Journal of Engineering Science* **133**, 109–131 (2018)
18. Kumar, S., Parks, D.M.: On the hyperelastic softening and elastic instabilities in graphene. *Proceedings of the Royal Society A: Mathematical, Physical and Engineering Sciences* **471**(2173), 20140567 (2015)
19. Lee, C., Wei, X., Kysar, J.W., Hone, J.: Measurement of the elastic properties and intrinsic strength of monolayer graphene. *Science* **321**(5887), 385–388 (2008)
20. Li, C., Xiao, J., Guo, T., Fan, S., Jin, W.: Effects of graphene membrane parameters on diaphragm-type optical fibre pressure sensing characteristics. *Materials Research Innovations* **19**(sup5), S5–17 (2015)
21. Liu, G., Jin, W., Xu, N.: Graphene-based membranes. *Chemical Society Reviews* **44**(15), 5016–5030 (2015)
22. Lu, Q., Gao, W., Huang, R.: Atomistic simulation and continuum modeling of graphene nanoribbons under uniaxial tension. *Modelling and Simulation in Materials Science and Engineering* **19**(5), 054006 (2011)
23. Lu, Q., Huang, R.: Nonlinear mechanics of single-atomic-layer graphene sheets. *International Journal of Applied Mechanics* **1**(03), 443–467 (2009)
24. Miculescu, M., Thakur, V.K., Miculescu, F., Voicu, S.I.: Graphene-based polymer nanocomposite membranes: a review. *Polymers for Advanced Technologies* **27**(7), 844–859 (2016)
25. Multiphysics, C.: Introduction to COMSOL multiphysics®. COMSOL Multiphysics, Burlington, MA, accessed Feb 9, 2018 (1998)
26. Ni, Z., Bu, H., Zou, M., Yi, H., Bi, K., Chen, Y.: Anisotropic mechanical properties of graphene sheets from molecular dynamics. *Physica B: Condensed Matter* **405**(5), 1301–1306 (2010)
27. Papageorgiou, D.G., Kinloch, I.A., Young, R.J.: Mechanical properties of graphene and graphene-based nanocomposites. *Progress in Materials Science* **90**, 75–127 (2017)
28. Pelliciari, M., Pasca, D.P., Aloisio, A., Tarantino, A.M.: Size effect in single layer graphene sheets and transition from molecular mechanics to continuum theory. *International Journal of Mechanical Sciences* **214**, 106895 (2022)
29. Pelliciari, M., Tarantino, A.M.: Equilibrium paths for von Mises trusses in finite elasticity. *Journal of Elasticity* **138**(2), 145–168 (2020)
30. Pelliciari, M., Tarantino, A.M.: Equilibrium paths of a three-bar truss in finite elasticity with an application to graphene. *Mathematics and Mechanics of Solids* **25**(3), 705–726 (2020)
31. Pelliciari, M., Tarantino, A.M.: Equilibrium and stability of anisotropic hyperelastic graphene membranes. *Journal of Elasticity* **144**(2), 169–195 (2021)
32. Pelliciari, M., Tarantino, A.M.: A nonlinear molecular mechanics model for graphene subjected to large in-plane deformations. *International Journal of Engineering Science* **167**, 103527 (2021)
33. Pumerana, M.: Graphene-based nanomaterials for energy storage. *Energy & Environmental Science* **4**(3), 668–674 (2011)
34. Quanshui, Z., Boehler, J.P.: Tensor function representations as applied to formulating constitutive laws for clinotropic materials. *Acta mechanica sinica* **10**(4), 336–348 (1994)
35. Raccichini, R., Varzi, A., Passerini, S., Scrosati, B.: The role of graphene for electrochemical energy storage. *Nature Materials* **14**(3), 271–279 (2015)
36. Rafiee, M.A., Rafiee, J., Wang, Z., Song, H., Yu, Z.Z., Koratkar, N.: Enhanced mechanical properties of nanocomposites at low graphene content. *ACS Nano* **3**(12), 3884–3890 (2009)
37. Saiz-Bretín, M., Domínguez-Adame, F., Malyshev, A.V.: Twisted graphene nanoribbons as nonlinear nanoelectronic devices. *Carbon* **149**, 587–593 (2019)
38. Shen, H., Zhang, L., Liu, M., Zhang, Z.: Biomedical applications of graphene. *Theranostics* **2**(3), 283 (2012)
39. Tao, L.Q., Zhang, K.N., Tian, H., Liu, Y., Wang, D.Y., Chen, Y.Q., Yang, Y., Ren, T.L.: Graphene-paper pressure sensor for detecting human motions. *ACS nano* **11**(9), 8790–8795 (2017)
40. Wang, D., Fan, S., Jin, W.: Graphene diaphragm analysis for pressure or acoustic sensor applications. *Microsystem technologies* **21**(1), 117–122 (2015)
41. Wang, M.C., Yan, C., Ma, L., Hu, N., Chen, M.W.: Effect of defects on fracture strength of graphene sheets. *Computational Materials Science* **54**, 236–239 (2012)
42. Wang, P., Gao, W., Cao, Z., Liechti, K.M., Huang, R.: Numerical analysis of circular graphene bubbles. *Journal of Applied Mechanics* **80**(4), 040905 (2013)
43. Wang, Q., Hong, W., Dong, L.: Graphene “microdrums” on a freestanding perforated thin membrane for high sensitivity MEMS pressure sensors. *Nanoscale* **8**(14), 7663–7671 (2016)
44. Yanovsky, Y.G., Nikitina, E.A., Karnet, Y.N., Nikitin, S.M.: Quantum mechanics study of the mechanism of deformation and fracture of graphene. *Physical Mesomechanics* **12**(5-6), 254–262 (2009)
45. Yuan, J., Liu, X., Xia, H., Huang, Y.: Analytical solutions for inflation of pre-stretched elastomeric circular membranes under uniform pressure. *Theoretical and Applied Mechanics Letters* p. 100243 (2021)
46. Zang, X., Zhou, Q., Chang, J., Liu, Y., Lin, L.: Graphene and carbon nanotube (CNT) in MEMS/NEMS applications. *Microelectronic Engineering* **132**, 192–206 (2015)
47. Zhao, H., Min, K., Aluru, N.R.: Size and chirality dependent elastic properties of graphene nanoribbons under uniaxial tension. *Nano Letters* **9**(8), 3012–3015 (2009)
48. Zhu, S.E., Krishna Ghatkesar, M., Zhang, C., Janssen, G.C.A.M.: Graphene based piezoresistive pressure sensor. *Applied Physics Letters* **102**(16), 161904 (2013)